Competing multiple-q magnetic structures in $HoGe_3$: II. Magnetic structures observed in $HoGe_3$

2008 J. Phys.: Condens. Matter 20 195202

(http://iopscience.iop.org/0953-8984/20/19/195202)

J. Phys.: Condens. Matter **20** (2008) 195202 (13pp) doi:10.1088/0953-8984/20/19/195202

Competing multiple-q magnetic structures in $HoGe_3$: II. Magnetic structures observed in $HoGe_3$

P Schobinger-Papamantellos[1], J Rodríguez-Carvajal[2], L D Tung[3], C Ritter[2] and K H J Buschow[4]

[1] Laboratory of Crystallography, ETH-Zurich, 8093 Zürich, Switzerland
[2] Institut Laue-Langevin, 156X, 38042 Grenoble Cédex, France
[3] Department of Physics, University of Liverpool, L69 7ZE, UK
[4] Van der Waals-Zeeman Institute, University of Amsterdam, NL-1018 XE, Amsterdam, The Netherlands

E-mail: Schobinger@mat.ethz.ch and JRC@ill.fr

Received 14 November 2007, in final form 21 February 2008
Published 8 April 2008
Online at stacks.iop.org/JPhysCM/20/195202

Abstract

The high temperature (HT) and the low temperature (LT) multiple-$\boldsymbol{q}$ vector magnetic structures of the antiferromagnetic $HoGe_3$ compound ($T_N = 11$ K) are derived from refinements of high resolution neutron data in terms of Fourier analysis. Various models are discussed. Over the HT range $T_2 \rightarrow T_N$, $T_2 = 8.1$ K (on heating), the magnetic phase is described with the wavevectors ($\boldsymbol{q}_1$, $\boldsymbol{q}_2$) where $\boldsymbol{q}_1 = (q_{1x}, 0, 0)$ and $\boldsymbol{q}_2 = (q_{2x}, 0, q_{2z})$, $q_{1x} = q_{2x} \approx \frac{1}{2}$ and $q_{2z} \approx \frac{1}{3}$, with T dependent length. It corresponds to an amplitude modulated magnetic phase with the moments at an angle of 24° (2) with the c axis within the plane (b, c). Surprisingly this structure does not square up to a constant moment structure with $\boldsymbol{q}_1 = (\frac{1}{2}, 0, 0)$ and $\boldsymbol{q}_2 = (\frac{1}{2}, 0, \frac{1}{3})$ or alternatively ($2a$, b, $3c$). Instead of locking, the $\boldsymbol{q}_2$ vector jumps at T_2 via a first-order transition to a long period structure with an almost 24-times larger cell $\approx(2a, 4b, 3c)$, or in terms of wavevectors to $\boldsymbol{q}_3 = (\frac{1}{2}, q_{3y}, 0)$ and $\boldsymbol{q}_4 = (\frac{1}{2}, q_{4y}, \frac{1}{3})$, which dominates the (LT) range 1.6 K $\rightarrow T_2$. The (LT) range subdivides into the lock-in LT_1 range 1.6 K $\rightarrow T_3$ ($T_3 = 4.8$ K on heating) where the $q_{3y} = q_{4y} = \frac{1}{4}$ components have a constant length and the LT_2 range $T_3 \rightarrow T_2$ where q_{3y} and q_{4y} have a length variable with T. In the intermediate temperature range, around the first-order T_2 transition (on heating or cooling), the two structures described with the wavevectors ($\boldsymbol{q}_1$, $\boldsymbol{q}_2$) and ($\boldsymbol{q}_3$, $\boldsymbol{q}_4$) coexist in varying proportions. The most probable LT magnetic structure corresponds to a complex monoclinic multiaxial canted structure with four independent Ho sites as a result of geometric frustration related to the underlying trigonal prism arrangement of the magnetic atoms with antiferromagnetic interactions.

(Some figures in this article are in colour only in the electronic version)

1. Introduction

Part I of the paper summarizes the physical properties and the results of a model independent analysis of high resolution neutron powder diffraction data for the $HoGe_3$ antiferromagnetic ($T_N = 11$ K) compound. This analysis led to a rather complex magnetic phase diagram (figure 12, part I) comprising two main regions of magnetic ordering: (i) a high temperature range and a (ii) low temperature range. These two regions are characterized by two multiple-$\boldsymbol{q}$ vector magnetic structures with symmetry independent wavevectors, and the transition among them at T_2 is of first order. A hysteresis width of 1.5 K is observed for T_2 depending on whether this temperature is determined from data obtained by heating $T_2^H = 8.1$ K or cooling $T_2^C = 6.6$ K; this is denoted by the superscripts H and C.

Long range magnetic ordering appears just below the Néel transition temperature $T_N = 11$ K, in agreement with the

magnetization and specific heat measurements. The latter transition is of second order, no hysteresis phenomena being observed between neutron data obtained by heating or cooling. The magnetic ordering is manifested by the appearance of the wavevector $\boldsymbol{q}_2 = (q_{2x}, 0, q_{2z})$ that dominates the HT range $T_2 \rightarrow T_N$, $T_2^H = 8.1$ K and $T_2^C = 6.6$ K. At slightly lower temperature around $T_1 \approx 9.5$ K, a very weak reflection appears close to the position $(\frac{1}{2}, 1, 0)$ at $2\theta = 18.75°$ in the high intensity (D1B) data. We assign to it the wavevector $\boldsymbol{q}_1 = (q_{1x}, 0, 0)$. Its role is not yet unambiguously clarified as the available information is extracted from the behaviour of very weak and overlapping observations in the transition ranges. Therefore we assume that it participates in a narrow region of the HT phase.

The LT ordering is characterized by the wavevectors $\boldsymbol{q}_3 = (\frac{1}{2}, q_{3y}, 0)$ and $\boldsymbol{q}_4 = (\frac{1}{2}, q_{4y}, \frac{1}{3})$ appearing below the first-order transition $T_2^H = 8.1$ K at the cost of the HT $\boldsymbol{q}_1$ and $\boldsymbol{q}_2$ satellites, which disappear completely at lower temperatures (7.75 K in the present experiment), while the $\boldsymbol{q}_3$ and $\boldsymbol{q}_4$ satellite reflections dominate the LT range and exist down to the lowest measured temperature, 1.6 K. The coexistence range of the $\boldsymbol{q}_2$ and $(\boldsymbol{q}_3, \boldsymbol{q}_4)$ magnetic phases is 0.5 K around T_2^H and 0.8 K around T_2^C. A further first-order lock-in transition is observed at $T_3 = 4.8$ K. Below T_3 the vectors $\boldsymbol{q}_3 = (\frac{1}{2}, \frac{1}{4}, 0)$ and $\boldsymbol{q}_4 = (\frac{1}{2}, \frac{1}{4}, \frac{1}{3})$ have a constant length (LT_1 range), and above T_3 a length variable with T and $q_{3y} = q_{4y}$ (LT_2 range).

In the present part of our paper we develop a *model dependent analysis* of the neutron data concerning the magnetic ordering for the HT and LT ranges. It comprises symmetry analysis, model choice for various refinements of the HR neutron diffraction data and finally the derivation of magnetic structures from the refined Fourier coefficients. The results are compared to those for isomorphic $R\mathrm{Ge}_3$ systems for which neutron diffraction data are available.

2. Neutron diffraction

The refinements of the magnetic structures given in the present paper are based exclusively on high resolution D1A neutron diffraction patterns collected with two wavelengths.

The data collected with a larger wavelength of 2.99 Å and very good statistics provide the best resolved magnetic patterns and they are also used to detect the magnetic wavevector(s) and higher harmonics and resolve the large number of overlapping magnetic peaks. They are also used in magnetic refinements. The eighteen data sets are partly collected with a temperature step of 0.1 K.

The 1.9108 Å data, with a larger 2θ range, are used for eight selected temperatures for indexing of the magnetic reflections (see figures 1 and 5 in paper I) and simultaneous structural and magnetic refinements in order to check for possible structural transitions in the high angle part. The data analysis is done with the *FullProf* suite of programs [1]. The structure plots are obtained with the program *FullProf Studio* [2] incorporated in [1]. Results are given in the following sections.

3. Model dependent magnetic refinements

3.1. The high temperature range 8.1 $K < T <$ 11 *K, D1A 1.9108 Å data*

3.1.1. Refinements of the 10.28 K data, $\boldsymbol{q}_2 = (q_{2x}, 0, q_{2z})$. The $HoGe_3$ HT magnetic phase, stable over the range 8.1 K $\rightarrow$ 11 K, is described by the symmetry independent incommensurate wavevectors $(\boldsymbol{q}_1, \boldsymbol{q}_2)$ with $\boldsymbol{q}_1 = (q_{1x}, 0, 0)$, $q_{1x} \approx \frac{1}{2}$ and $\boldsymbol{q}_2 = (q_{2x}, 0, q_{2z})$, $q_{2x} \approx \frac{1}{2}$, $q_{2z} \approx \frac{1}{3}$ relating to the C-cell (a, b, c). Although the HT magnetic peak topology is similar to that of the $TbGe_3$ $(\boldsymbol{q}_1, \boldsymbol{q}_2)$ HT phase at 27 K [3], for $HoGe_3$ it differs in a few points, in particular with regard to the behaviour of the $\boldsymbol{q}_1$ vector (see for instance figure 8 in part I).

At 10.28 K no reflections associated with the wavevector $\boldsymbol{q}_1$ have been observed. As can be seen in figure 1, even at 9.31 K the first expected $\boldsymbol{q}_1$ peak (110) $- \boldsymbol{q}_1$ is not resolved from the background. The 10.28 K incommensurate structure is then described with a single Fourier coefficient pertaining to $\boldsymbol{q}_2$. The refined $\boldsymbol{q}_2$ components, obtained from the D1A 2.99 Å data at 10.28 K with the profile matching program tool, are $q_{2x} = 0.4933(1)$ and $q_{2z} = 0.3392(2)$. Fixing q_{2x} and q_{2z} to their commensurate values leads to a 2% increase of R_{wp}. This suggests that the HT magnetic structure is incommensurate with the crystal lattice and can be described with a single wavevector $\boldsymbol{q}_2$. The 10.28 K refined magnetic parameters are summarized in table 1. The refined magnetic structure shown in figure 2 corresponds to a collinear amplitude modulated structure with the moments confined to the (b, c) plane at an angle of 24°(2) to the c axis. The amplitude of the wave (Fourier coefficient) of 4.5(5) μ_B/Ho atom is strongly reduced below the free ion value $gJ\mu_B = 10\ \mu_B$ for Ho^{3+} most likely because of thermal disorder and coexisting short range order effects. Details for the HT magnetic structure will be discussed in the following sections.

3.1.2. Indexing and refinement of the 8.34 K $(\boldsymbol{q}_1, \boldsymbol{q}_2)$ *phase, D1A data.* The indexing of the 8.34 K magnetic reflections requires two wavevectors. We already mentioned that below $T_1 = 9.5$ K, in agreement with the anomaly observed in the specific heat (figure 4 C/T data, part I), a phase transition associated with a second wavevector $\boldsymbol{q}_1$ sets in. The appearance of a uniquely resolved peak close to the $(\frac{1}{2}, 1, 0)$ reciprocal lattice position marks the onset of this transition. This peak becomes more important at 8.34 K, but below $T_2^H = 8.1$ K it is no longer resolved in the 1.91 Å data. By the analogy with the $TbGe_3$ HT phase, we assume that this wavevector is $\boldsymbol{q}_1 = (q_{1x}, 0, 0)$ and relates to the $(\boldsymbol{q}_1, \boldsymbol{q}_2)$ HT modulated structure in a narrow range from T_1 and down to T_2. Its presence is a first sign that the HT phase became unstable and 'tried' to square up.

The data evaluation follows the results of symmetry analysis given extensively in [3] for the wavevectors $\boldsymbol{q}_1$ and $\boldsymbol{q}_2$ and the space group $Cmcm$. These results provide parameter relations (basis functions) between the components of the Fourier coefficients of the two atoms of the basis cell at the

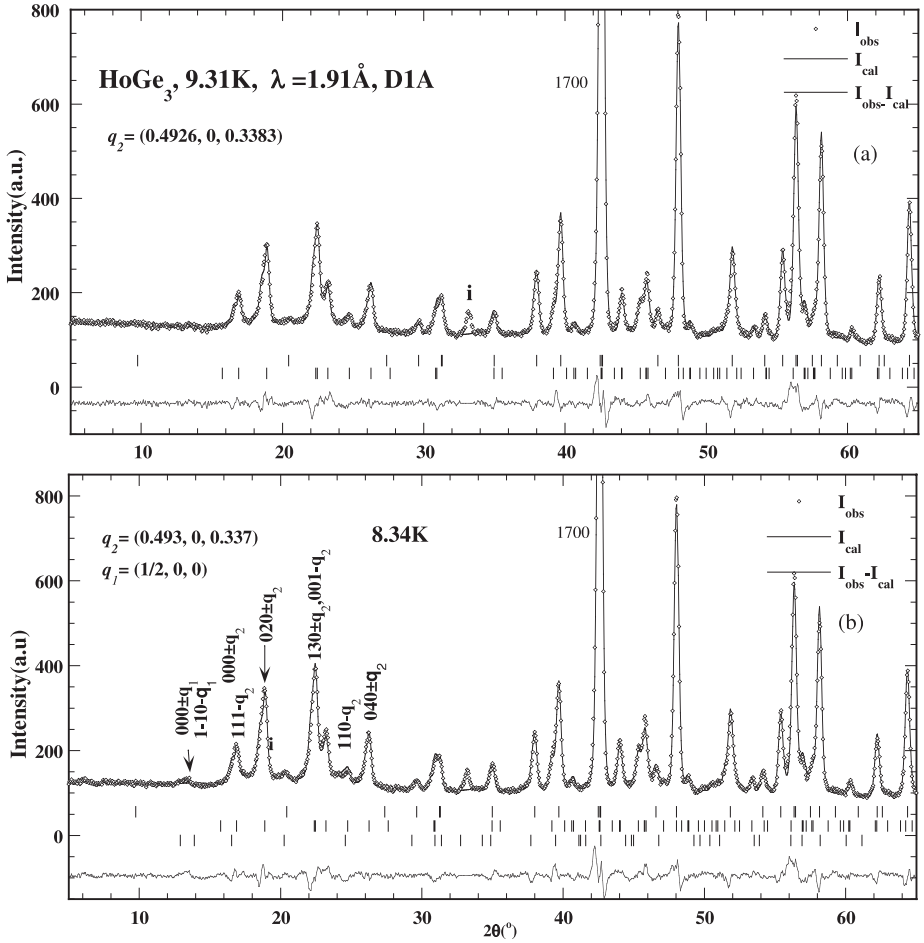

Figure 1. Parts of the observed and calculated neutron diffraction patterns for $HoGe_3$ (D1A 1.91 Å data): for the HT magnetically ordered state at 9.31 K (a), 8.34 K (b) with the magnetic vectors $\boldsymbol{q}_2$ and ($\boldsymbol{q}_1$, $\boldsymbol{q}_2$) respectively.

Table 1. Refined magnetic moment amplitudes for the $\boldsymbol{q}_1$ and $\boldsymbol{q}_2$ Fourier coefficients $S\boldsymbol{q}_i$, the phases, φ_{qi}, and the global phase, $\Psi_{\mathrm{G}}^{\mathrm{a}}$, for Ho1 at (0, y, $\frac{1}{4}$) and Ho2 at (0, $-y$, $\frac{3}{4}$) in the HT range (10.28 K, 9.31 K and 8.34 K) from neutron D1A data (1.91 Å) of $HoGe_3$. The moment angle to the c axis is $\varphi_c = 24°$ (2). The Ho3 and Ho4 atoms shifted by ($\frac{1}{2}$, $\frac{1}{2}$, 0) have the same moment values but opposite signs. R_{m}% is the agreement factor for the magnetic refinements. Calculated local moment values (right part) for 12 Ho atoms at 10.28 K. The labels correspond to those of figure 2.

Atom	$\varphi(\boldsymbol{q}_1)/\varphi(\boldsymbol{q}_2)$	$S_y(\boldsymbol{q}_j)$ (μ_{B})	$S_z(\boldsymbol{q}_j)$ (μ_{B})	$\lvert S(\boldsymbol{q}_j)\rvert$ (μ_{B})	Ψ_{G} φ_c°	R_{m}%	Atom figure 2	μ_y (μ_{B})	μ_z (μ_{B})	μ_T (μ_{B})
10.28 K, $q_{2x} = 0.4932(2)$, $q_{2z} = 0.3392(2)$						9	1	−0.87	−1.8	2.03
Ho1($\boldsymbol{q}_2$)	0	2.0(2)	4.0(1)	4.50(5)	0.639		1′	1.35	2.84	3.15
Ho2($\boldsymbol{q}_2$)	0.66(2)	2.0(2)	4.0(1)	4.50(5)	26(3)		1″	−0.56	−1.19	1.32
9.31 K, $q_{2x} = 0.4926(1)$, $q_{2x} = 0.3383(1)$						6.6	2	−0.40	−0.85	0.939
Ho1($\boldsymbol{q}_2$)	0	2.3(2)	5.7(6)	6.20(4)	0.639		2′	−0.89	−1.87	2.07
Ho2($\boldsymbol{q}_2$)	0.66(1)	2.3(2)	5.7(6)	6.20(4)	22(2)		2″	1.349	2.840	3.144
8.34 K, $q_{2x} = 0.4931(1)$, $q_{2x} = 0.3376(1)$						6.5	3	1.03	2.17	2.403
Ho1($\boldsymbol{q}_1$)	0	0	0.3(1)	0.3(1)	0.639		3′	0.209	0.439	0.487
Ho1($\boldsymbol{q}_2$)	0	2.8(1)	6.41(6)	7.01(3)	24(1)		3″	−1.25	−2.64	2.92
							4	−1.31	−2.76	3.06
							4′	1.015	2.14	2.366
Ho2($\boldsymbol{q}_1$)	0	0	0.3(1)	0.3(1)			4″	0.232	0.49	0.542
Ho2($\boldsymbol{q}2$)	0.68(1)	2.8(1)	6.41(6)	7.01(3)						

[a] φ_{qi} is the phase between Fourier components in fractions of 2π of magnetic moments of the same representation in the commensurate refinement fixed by symmetry. The total phase for each atom is obtained from the relation $\Phi_{Tj} = \varphi(\boldsymbol{q}_i) + \Psi_G$. Ψ_{G} are global phases in fractions of 2π (origin shift) of a given arrangement, obtained by optimization.

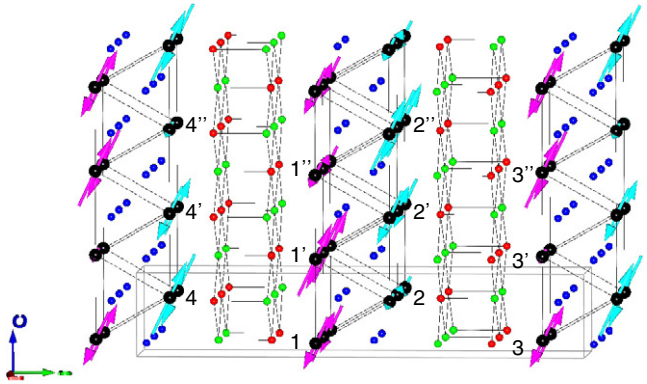

Figure 2. The collinear amplitude modulated magnetic structure of $HoGe_3$ at 10.28 K for a few cells along the c direction. The moment value varies over 0.5 → 3.15 μ_B/atom depending on the position; see table 1 (right part).

4c symmetry site for the two wavevectors:

$$\text{Ho at } 4c, m2m\text{: Ho1: } (0, y, 1/4); \text{ Ho2: } (0, -y, -1/4),$$

$$y = 0.417.$$

The 8.34 K refined data show that the moment angle with the c axis remains, within experimental error, unchanged going down with temperature. The main difference from the 10.28 K results is the Sq_1 Fourier coefficient. Using the same model as for the $TbGe_3$ (q_1, q_2) phase we find an increase of the refined moment amplitude Sq_2 from 4.5(5) μ_B/Ho at 10.28 K to 7.0(3) μ_B/Ho atom at 8.34 K, while Sq_1 is negligible, 0.33(1) μ_B/Ho, and its refinement is unstable. Most likely the behaviour of the $TbGe_3$ HT fluctuating sinusoidal model does not apply for $HoGe_3$. We show the refined neutron patterns at 9.31 K and 8.34 K in figure 1. The refinements of the q_1 contributions are restricted just to the low angle ($2\theta < 60°$) range for obvious reasons and are visible only at 8.34 K. Results are given in table 1. The magnetic reliability factors (6 → 9%) are satisfactory. The structural parameters have been given in table 1, part I.

3.1.3. The HT magnetic structures. The incommensurate q_1 and q_2 magnetic structures correspond to sinusoidal modulated structures. At 8.34 K the refined Fourier coefficients are 0.33(1) μ_B for q_1 and 7.0(3) μ_B/Ho atom for q_2 (table 1). The real structure for each independent system may be derived by Fourier expansion from the refined Fourier coefficients $S_\nu(q_j)$ of the magnetic moments in the basic unit cell (table 1) using the expression

$$m_\nu(\boldsymbol{R}_n) = \sum_{\{j\}} S_\nu(\boldsymbol{q}_j) \exp(-2\pi i \boldsymbol{q}_j \cdot \boldsymbol{R}_n)$$
$$= \sum_j S_\nu^R(\boldsymbol{q}_j) \cos\{2\pi \boldsymbol{q}_j \cdot \boldsymbol{R}_n + \varphi_{j\nu}\} \quad (1)$$

$$m'_\nu(\boldsymbol{R}_n) = \sum_{\{j\}} S_\nu(\boldsymbol{q}_j) \exp(-2\pi i \boldsymbol{q}_j \cdot \boldsymbol{R}_n + \Psi_G) \quad (1')$$

where $\boldsymbol{R}_{n\nu} = \boldsymbol{r}_\nu + \boldsymbol{R}_n$ are the moment positions and $\boldsymbol{R}_n = n_1\boldsymbol{a} + n_2\boldsymbol{b} + n_3\boldsymbol{c}$ is a lattice translation vector with n_3 always integer and (n_1, n_2) integer or simultaneously half-integers (for the C-centred lattice); $\boldsymbol{r}_\nu$ is the vector position of the atom ν in a primitive unit cell (in our case $\nu = 1, 2$).

The first sums extend for all pairs $(\boldsymbol{q}_j, -\boldsymbol{q}_j)$ of propagation vectors. The last sum assumes that the Fourier coefficients have the form $S_\nu(\boldsymbol{q}_j) = \frac{1}{2} S_\nu^R(\boldsymbol{q}_j) e^{-i\varphi_{j\nu}}$ so that only cosine terms appear after grouping the pairs $(\boldsymbol{q}_j, -\boldsymbol{q}_j)$. The global phase Ψ_G is a free parameter not depending on symmetry. The phases $\varphi_\nu(\boldsymbol{q}_j) = \varphi_{j\nu}$ between atoms of the same orbit are deduced by symmetry analysis from the basis functions of the representation [3]. These are usually products of the wavevectors with the translation part of the symmetry operators of G_q and/or returning translations. In commensurate phases these are fixed. If there is more than one orbit, an additional phase between the orbits has to be refined.

The amplitudes of the Fourier coefficients of the q_1 magnetic phase are strongly reduced below the free ion value. In principle the q_1 and q_2 Fourier coefficients describe two independent magnetic systems coexisting in the form of domains.

Alternatively one may assume that the two wavevectors act on the same physical space. In this case the real structure has to be derived using equation (1) by adding up all observed Fourier coefficients. Applying this to the 8.34 K data one derives maximal amplitude of 7.3(3) μ_B/Ho atom. Compared to that of the 9.31 K ($Sq_2 = 6.2(4)$ μ_B/Ho atom; see table 1) one finds a 15% increase. Because of the doubts concerning the Sq_1 Fourier component at 8.34 K and its negligible contribution we restrict ourselves to showing the modulated structure at 10.28 K (figure 2).

When a structure has various vectors $\boldsymbol{q}$, it is not always possible to derive the spin configuration because the phase between the various Fourier coefficients cannot be found by diffraction methods [4]. The reason is that the addition of a global phase Ψ_G depending on $\boldsymbol{q}$ modifies the magnetic structure, through origin shifts of the waves $\boldsymbol{q}$, without changing the magnetic intensities. The moment distribution given by equation (1′) gives the same diffraction pattern as that of equation (1). Figure 2 shows the magnetic structure at 10.28 K optimized using the program '*Moment*' for a limited region of the crystal. In fact this program makes a phase search (Ψ_G) for a given periodic magnetic moment distribution (commensurate with the crystal lattice) in order to minimize the fluctuation in the local magnetic moment values resulting from the refined Fourier coefficients using formula (1). This corresponds to the addition of a global phase Ψ_G in fractions of 2π (origin shift in formula (1′)) of the wave describing a given periodic arrangement. For incommensurate sine wave magnetic structures the addition of a global phase may only have an influence on the moment fluctuations in a small part of the crystal and not in a larger area, as the structure remains incommensurate.

Thus the calculated amplitude modulated structure displayed in figure 2 at 10.28 K for the wavevector $\boldsymbol{q}_2 = (0.4932(2), 0, 0.3392(2)) \approx (0, \frac{1}{2}, \frac{1}{3})$ is obtained from the refined Fourier coefficients of the Ho1 and Ho2 atoms in the basis cell (4.5 μ_B/atom; see table 1) when a global phase of $\Psi_G = 0.639 \times 2\pi$ is inserted in (1) and $\Phi_T = \varphi(\boldsymbol{q}_i) + \Psi_G$.

Table 2. Atomic positions in the $Pmcm$ setting $(2a, b, 3c)$. The 24 Ho atoms occupy six Wyckoff sites: Ho1′: $4i$ $(0, 0.41, \frac{1}{12})$ Ho2′: $4j$ $(\frac{1}{12}, \frac{1}{2}, 0.41)$; Ho3′: $8l$ $(\frac{1}{4}, 0.91, \frac{1}{12})$; Ho4′: $2e$ $(0, 0.59, \frac{1}{4})$; Ho5′: $2f$ $(\frac{1}{2}, 0.59, \frac{1}{4})$; Ho6′: $4k$ $(\frac{1}{4}, 0.09, \frac{1}{4})$. Columns $1 \rightarrow 3$ give the atomic positions correlated through constraints imposed in the magnetic refinements. Each of the six sites splits into two orbits (1 and 2) under the action of the wavevector $(0, \frac{1}{4}, 0)$. Atom numbers relate to the international settings and are in bold for orbit 1.

			Site		Ho1		Site		Ho2		Site		Ho3		Site		Ho4	
x	y	z	Orbit 1	x	y	z	Orbit 2	x	y	z	Orbit 1	x	y	z	Orbit 2	x	y	z
0	y	z	$4i$: **1**	0	0.41	1/12	$4i$: 4	0	0.59	7/12	$2e$: **1**	0	0.59	1/4	$2e$: 2	0	0.41	3/4
0	y	$\bar{z}+1/2$	**2**	0	0.41	5/12	3	0	0.59	11/12								
1/2	y	z	$4j$: **1**	1/2	0.41	1/12	$4j$: 4	1/2	0.59	7/12	$2f$: **1**	1/2	0.59	1/4	$2f$: 2	1/2	0.41	3/4
1/2	y	$\bar{z}+1/2$	**2**	1/2	0.41	5/12	3	1/2	0.59	11/12								
1/4	$y+1/2$	z	$8l$: **1**	1/4	0.91	1/12	$8l$: 6	1/4	0.09	7/12	$4k$: **1**	1/4	0.09	1/4	$4k$: 3	1/4	0.91	3/4
1/4	$y+1/2$	$\bar{z}+1/2$	**8**	1/4	0.91	5/12	3	1/4	0.09	11/12								
3/4	$y+1/2$	z	**7**	3/4	0.91	1/12	4	3/4	0.09	7/12	**2**	3/4	0.09	1/4	4	3/4	0.91	3/4
3/4	$y+1/2$	$\bar{z}+1/2$	**2**	3/4	0.91	5/12	5	3/4	0.09	11/12								

Table 3. Irreducible representations and magnetic modes for orbit 1 of the sites $8l, 4i, 4j$, and $4k$ that split into two orbits under the action of the vector $q = (0, \frac{1}{4}, 0)$ in $Pmcm$ (51); see table 2. The symbols for the magnetic modes are: $A(+\,-\,-+)$; $G(+\,-\,+-)$: $C(+\,+\,--)$ and $F(+\,+\,++)$ for the $8l$ site and $A(+-)$ and $F(++)$ for the $4i, 4j$ and $4k$ sites in the sequence given in table 2. The moments of the atoms of the orbits of $2e$ and $2f$ sites point along y, z and x for the representations Γ_2, Γ_3, Γ_4 respectively. Also given are the observed modes corresponding to two different representations.

					$8l$			$4i$			$4j$			$4k$		
Irrep	$(1\|0)$	$(2_y\|001/2)$	$(m_z\|001/2)$	$(m_x\|0)$	x	y	z	x	y	z	x	y	z	x	y	z
Γ_1	1	1	1	1	Gx	Ay	Cz	Ax			Ax					Az
Γ_2	1	1	−1	−1	Cx	Fy	Gz		Fy	Az		Fy	Az	Ax	Fy	
Γ_3	1	−1	1	−1	Ax	Gy	Fz		Ay	Fz		Ay	Fz			Fz
Γ_4	1	−1	−1	1	Fx	Cy	Az	Fx			Fx			Fx	Ay	
Observed modes					Γ_1	Ay	Cz	Γ_3	Ay	Fz	Γ_3	Ay	Fz	Γ_1		Az

The moment values in figure 2 for a large number of cells $(2\times a, b, 4\times c)$ are given in the right part of table 1. We use the same labels as in figure 2. The magnetic moment value varies over $0.5 \rightarrow 3.2\ \mu_B$/Ho atom. The moments of the atoms 3 and 4 shifted by $(\frac{1}{2}, \frac{1}{2}, 0)$ from those of 1 and 2 are almost equal to those of 1 and 2 but with opposite sign. As the temperature goes down, the refined Fourier coefficients increase and the local values increase, though the global phase is the same. The structure remains incommensurate and the ordered local moment value is position dependent in the direction of the wavevector and constant in planes perpendicular to it.

3.2. The low temperature range 1.6 K < T < 8.1 K, D1A 1.9108 Å data

The indexing of the magnetic satellites in the LT range led to a 24-times larger cell. The huge number of reflections produced in the $(2a, 4b, 3c)$ commensurate cell imply a situation close to the limits of powder diffraction. Alternatively we make use of two models in terms of Fourier coefficients with different wavevectors and basis. Model (I) has a single wavevector $\boldsymbol{q} = (0, q_y, 0)$ with $q_y \approx \frac{1}{4}$ and relates to the $(2a, b, 3c)$ P-cell. Model (II) uses two wavevectors $(\boldsymbol{q}_3, \boldsymbol{q}_4)$, $\boldsymbol{q}_3 = (\frac{1}{2}, q_{3y}, 0)$, $\boldsymbol{q}_4 = (\frac{1}{2}, q_{4y}, \frac{1}{3})$ $q_{3y} = q_{4y} \approx \frac{1}{4}$ and relates to the (a, b, c) C-cell. The wavevector star of $\boldsymbol{q}_3$ and $\boldsymbol{q}_4$ has four and eight branches respectively. The latter model produces the minimum number of reflections (1330). In model (II) the Ho site splits into two orbits for each of the two vectors and is described by a single representation for $\boldsymbol{q}_4$ with (m_x, m_y, m_z) moment components and with two representations for $\boldsymbol{q}_3$, one allowing only m_z uniaxial moment arrangements, the other planar (m_x, m_y). Our refinements make use of both. Model (I) led to better fits as the number of free parameters increased from 4 against 1330 reflections to 5 against 7930 reflections. In the following we will show the refined structures for the calculations for comparison and discuss the results together with the refinements carried on the better resolved 2.99 Å D1A data. These data are also used for the refinement of the wavevector components versus T for a full set of temperatures.

3.2.1. Symmetry analysis for model (I).

Propagation vector $\boldsymbol{q} = (0, \frac{1}{4}, 0)$ $Pmcm(2a, b, 3c)$. Model (I) relates to the primitive enlarged cell $(2a, b, 3c)$ in the non-standard space group $Pmcm$ (No 51) and the wavevector $(0, \frac{1}{4}, 0)$. The 24 Ho atoms in this setting (see table 2) occupy six distinct Wyckoff sites: Ho1′: $4i$ $(0, 0.41, \frac{1}{12})$, Ho2′: $4j$ $(\frac{1}{12}, \frac{1}{2}, 0.41)$; Ho3′: $8l$ $(\frac{1}{4}, 0.91, \frac{1}{12})$; Ho4′: $2e$ $(0, 0.59, \frac{1}{4})$; Ho5′: $2f$ $(\frac{1}{2}, 0.59, \frac{1}{4})$; Ho6′: $4k$ $(\frac{1}{4}, 0.09, \frac{1}{4})$. Atom sites relate to the international settings.

The point group of $\boldsymbol{q}$ is $G_1^0 = m2m = \{1, m_x, 2_y, mz\}$ which has four one-dimensional representations. The magnetic structure can be described by any of these four representations or any linear combination among them. The star of $\boldsymbol{q}$ has two arms: $(\boldsymbol{q}, -\boldsymbol{q})$. The representations of the space group of $\boldsymbol{q}$, $G = Pm2m$, are obtained from those of G_1^0 using the expression

$$D^{\gamma}(h|\boldsymbol{t}_h) = \mathrm{e}^{-2\pi \mathrm{i}\boldsymbol{q}\boldsymbol{t}_h} D^{0\gamma}(h). \qquad (2)$$

The coset representatives of G with respect to the translation group are $(1|0)$, $(2_y|001/2)$, $(m_x|0)$, $(m_y|001/2)$. Due to the particular form of the translations the products $\boldsymbol{q}\boldsymbol{t}_h$

Table 4. The signs of the observed moment components (u, v, w) of the 24 Ho atoms distributed over the twelve magnetic orbits associated with the six Wyckoff sites and the wavevector $(0, \frac{1}{4}, 0)$: Ho1′: $4i$ $(0, 0.41, \frac{1}{12})$ Ho2′: $4j$ $(\frac{1}{12}, \frac{1}{2}, 0.41)$; Ho3′: $8l$ $(\frac{1}{4}, 0.91, \frac{1}{12})$; Ho4′: $2e$ $(0, 0.59, \frac{1}{4})$; Ho5′: $2f$ $(\frac{1}{2}, 0.59, \frac{1}{4})$; Ho6′: $4k$ $(\frac{1}{4}, 0.09, \frac{1}{4})$.

			Site		Ho1		Site		Ho2		Site		Ho3		Site		Ho4	
x	y	z	Orbit 1	u	v	w	Orbit 2	u	v	w	Orbit 1	u	v	w	Orbit 2	u	v	w
0	y	z	$4i$: **1**		+	+	$4i$: 4		+	+	$2e$: **1**			+	$2e$: 2			+
0	y	$\bar{z}+1/2$	**2**		−	+	3		−	+								
1/2	y	z	$4j$: **1**		−	−	$4j$: 4		−	−	$2f$: **1**			−	$2f$: 2			−
1/2	y	$\bar{z}+1/2$	**2**		+	−	3		+	−								
1/4	$y+1/2$	z	$8l$: **1**		−	−	$8l$: 6		−	−	$4k$: **1**			−	$4k$: 3			−
1/4	$y+1/2$	$\bar{z}+1/2$	**8**		+	−	3		+	−								
3/4	$y+1/2$	z	**7**		+	+	4		+	+	**2**			+	4			+
3/4	$y+1/2$	$\bar{z}+1/2$	**2**		−	+	5		−	+								

are zero and the matrices D^{γ} are identical to $D^{0\gamma}$. Under the action of the wavevector $(0, \frac{1}{4}, 0)$ each of the six Ho sites splits into two orbits in the way given in table 2. Atom numbers of orbit 1 are in bold.

In table 3 we give the representations and the basis functions corresponding to four of the Ho sites, $8l$, $4i$, $4j$ and $4k$, and the propagation vector $\boldsymbol{q}$. The orbits of sites $2e$ and $2f$ harbour a single atom and are not given explicitly. The basis functions $F(++++)$, $A(+--+)$, $C(++--)$ and $G(+-+-)$ give the signs of the Fourier components $S_{q\nu}$ of the $(\nu = 1, \ldots, 4)$ Ho atoms for the orbits of the $8l$ site. The signs of the modes F, A, C and G relate to the atoms in the sequence given in table 2. For instance, for the atoms (1, 2) of orbit 1 of the $4k$ site the Fourier components of the representation Γ_1 are of the form of the $A_x(+-)$ mode:

$$S_{q1} = (u, 0, 0) \quad \text{and} \quad S_{q2} = (-u, 0, 0).$$

Atoms (3, 4) belong to the second orbit which has the same mode but may have different moment value. The same basis functions correspond to the other arm of the star. Thus the magnetic structure for this site corresponds to a modulated structure with atoms 1 and 2 for orbit 1 in antiphase within the reference cell. The same holds for orbit 2.

Symmetry analysis shows that the atoms of orbits 1 and 2 of the $8l$ site may have three magnetic components, while those of the orbits of the $4i$, $4j$ and $4k$ sites may have either one or two components. Finally the $2e$ and $2f$ orbits not included in table 2 may only have a component along the axes y, z and x in the representations Γ_2, Γ_2, Γ_4 respectively. The parameter reduction resulting from the symmetry analysis is used in the refinements of various models.

Additional parameter constraints used in model (I). Further parameter constraints are inserted in our refinements through the simple assumption that the LT commensurate magnetic structure maintains some of the characteristics of the HT phase as the $(2a, b, 3c)$ enlarged cell corresponds to the lock-in value of the HT incommensurate structure described with $\boldsymbol{q}_1 \approx (\frac{1}{2}, 0, 0)$ and $\boldsymbol{q}_2 \approx (\frac{1}{2}, 0, \frac{1}{3})$ and $Cmcm$ space group (a, b, c).

In the incommensurate phase the moments of atoms shifted by t_a and by the non-primitive translation $(\frac{1}{2}, \frac{1}{2}, 0)$ have opposite signs but slightly different values. In the lock-in phase in the sixfold-enlarged cell $(2a, b, 3c)$ with $Pmcm$ symmetry and the wavevector $\boldsymbol{q} = (0, \frac{1}{4}, 0)$ these two constraints correspond to parameter correlations between the moments of atoms of any of the six magnetic Ho sites and those shifted by $(\frac{1}{2}, 0, 0)$ and $(\frac{1}{4}, \frac{1}{2}, 0)$ to have opposite signs and the same moment value.

These constraints are given in columns $1 \rightarrow 3$ of table 2 and it is evident that they provide a significant parameter reduction. Thus the twelve Ho magnetic orbits are regrouped into four independent Ho_{ν} sites $(\nu = 1, \ldots, 4)$ given at the top of the corresponding columns. Each of these sites is composed of one orbit of three distinct sites: Ho1 comprises orbit 1 of the $4i$, $4j$ and $8l$ sites while Ho2 comprises orbit 2 of the same sites. Ho3 and Ho4 sites comprise orbit 1 and orbit 2 of the group of $2e$, $2f$ and $4k$ sites, respectively.

The best fit is found for a model where the ordering of half of the Ho atoms in the cell comprising the two orbits of the 8l and 4k sites is described by the Γ_1 representation, while the other half, comprising the orbits of the 4i, 4j, 2e and 2f sites, is described by Γ_3. This indicates a further symmetry reduction to the monoclinic space group $P11m$.

The refinement converged for equal values of the Fourier coefficients for the (eightfold) Ho1 and Ho2 sites and equal values of the (fourfold) sites Ho3 and Ho4. Because of the large number of atoms we give explicitly the signs of the observed modes for all atoms in the cell in table 4. The refined parameters are then given in tables 5a, 5b and 6 for a full set of temperatures. Figures 3 and 4 (top part) show two characteristic refined patterns of the LT_2 range that will be discussed below. The refined lock-in structure is shown in figure 5(a) at 1.6 K.

3.2.2. *LT magnetic refinements of the D1A 2.99 Å data.*

The LT_2 range ($T_3 = 4.8$ K $\rightarrow$ $T_2 = 8.1$ K). The refinements of the LT 1.9108 Å data based on model (I) ($\boldsymbol{q} = (0, \frac{1}{4}, 0)$ relating to the $(2a, b, 3c)$ P-cell; see table 6) led to a modulated canted moment arrangement. However due to the large number of overlapping magnetic peaks, strong correlation exists between moment values and background. Furthermore from the D1B LT data we got an indication that the q_y component is slightly incommensurate with the crystal lattice over the LT_2 range 4.8 K $\rightarrow$ 8.1 K. For this reason we focus on the results of the LT_2 refined D1A patterns collected

Table 5a. Refinements of HR D1A data for $HoGe_3$ in the HT range with wavevector $\boldsymbol{q}_2 = (q_{2x}, 0, q_{2z})$ relating to C-cell (a, b, c) and the LT range with (model (I)) $\boldsymbol{q} = (0, q_y, 0)$ relating to the enlarged P-cell $(2a, b, 3c)$. $\boldsymbol{Sq}_i$ are the Fourier coefficients and $\varphi_{Sq}c^\circ$ their angles with c, $\varphi\boldsymbol{Sq}_i$ the phases among the various orbits (in fractions of 2π). Also given is the percentage of observed $\boldsymbol{q}_2$ and $\boldsymbol{q}$ magnetic intensities (161 and 2182 reflections respectively).

No	$\lambda = 2.99$ Å T (K)	q_{2x} q_{2z} (a, b, c)	$\boldsymbol{Sq}_2$ $\varphi S\boldsymbol{q}_2c^\circ$	q_y $(2a, b, 3c)$	$\boldsymbol{Sq}_{\mathrm{Ho1,Ho2}}$ $\boldsymbol{Sq}_{\mathrm{Ho3,Ho4}}$	$\varphi\boldsymbol{Sq}_{\mathrm{Ho3}}$ $\varphi\boldsymbol{Sq}_{\mathrm{Ho4}}$	$\varphi\boldsymbol{Sq}c^\circ_{\mathrm{Ho1,Ho2}}$ $\varphi\boldsymbol{Sq}c^\circ_{\mathrm{Ho3,Ho4}}$	Int $\boldsymbol{q}_2$ Int $\boldsymbol{q}$%		R_{B}, R_{wp}, R_{exp}%, χ^2	R_{mq2}, R_{mq}%
1	1.66			0.25	11.4(1.0)	0.467(10)	44(1)	—		2.4, 14.1	—
					5.2(5)	0.448(13)	0	41		5.5, 6.6	7.1
2	3.43			0.25	11.3(1.0)	0.464(10)	46(1)	—		2.7, 14.2	—
					5.3(7)	0.427(13)	0	41	T_3	4.7, 8.9	7.5
3	5.35			0.2565(3)	10.3(8)	0.487(9)	35(1)	—		2.3, 13.7	—
					6.8(7)	0.502(10)	0	39		5.7, 5.8	7.8
4	5.83			0.2585(3)	10.0(8)	0.485(9)	36(1)	—		2.3, 13.7	—
					6.8(6)	0.505(10)	0	38		5.7, 5.7	7.9
5	6.3			0.2602(2)	9.7(8)	0.486(9)	34(1)	—		2.0 13.5	—
					7.1(6)	0.512(10)	0	37		5.8, 5.4	7.4
6	6.77			0.2624(2)	9.3(8)	0.488(9)	34(1)	—		2.2, 13.8	—
					7.3(6)	0.511(10)	0	36		5.9, 5.5	7.8
7	7.24			0.2642(2)	8.9(7)	0.488(9)	35(1)	—		2.1, 13.6	—
					7.2(6)	0.519(10)	0	34		6.0, 5.2	7.8
8	7.71			0.2649(3)	8.3(7)	0.496(9)	40(1)	—		3.0, 15.1	—
					6.6(6)	0.528(11)	0	31		6.1, 6.1	9.3
9	7.80	0.4959(5)	1.8(1) 25(18)	0.2623(3)	7.6(7)	0.542(9)	44(1)	1.6		3.0, 14.4	20
		0.3355(7)			6.6(6)	0.582(11)	0	28		6.2, 5.4	8.7
10	7.89	0.4947(2)	3.0(6) 22(7)	0.2619(3)	6.9(5)	0.538(11)	44(1)	4.5		2.5, 12.8	12.9
		0.3353(2)			5.6(4)	0.561(15)	0	23		6.3, 4.1	10.2
11	7.99	0.4945(1)	4.47(4) 20(3)	0.2602(5)	6.2(3)	0.543(16)	47(2)	9.9		2.6, 13.0	8.8
		0.3348(1)			4.1(4)	0.590(20)	0	17		6.0, 4.2	12.4
12	8.08	0.4940(1)	5.55(4) 20(2)	0.2579(9)	5.3(4)	0.615(32)	52(3)	15.4	T_2	2.7, 13.6	9.2
		0.3347(1)			2.5(4)	0.774(42)	0	11.1		6.1, 4.9	—
13	8.17	0.4935(1)	6.27(4) 26(2)	—				21.4		2.8, 14.4	9.1
		0.3351(1)						—		6.3, 5.2	—
14	8.64	0.4931(1)	6.78(4) 23(2)					23.8		2.5, 12.5	6.5
		0.3355(1)						—		6.0, 4.5	—
15	9.10	0.4928(1)	6.45(3) 21(2)					22	T_1	2.4, 12.2	6.6
		0.3356(1)						—		6.1, 4.2	—
16	10.01	0.4930(1)	5.35(4) 22(2)					16.3		2.6, 11.9	6.1
		0.3358(1)						—		6.4, 3.7	—
17	10.90	0.4953(3)	2.47(5) 36(5)					3.8	T_N	2.4, 11.3	15.2
		0.3385(3)						—		4.9, 5.4	—
18	14.0							—		2.5, 11.9	—
								—		6.1, 3.7	—

Table 5b. Refinements of HR D1A $HoGe_3$ data in the LT range with (model (II)), $\boldsymbol{q}_3 = (\frac{1}{2}, q_{3y}, 0)$, $\boldsymbol{q}_4 = (\frac{1}{2}, q_{4y}, \frac{1}{3})$ phase, relating to the C-cell (a, b, c). $\boldsymbol{Sq}_i$ are the Fourier coefficients and $\varphi\boldsymbol{Sq}c^\circ$ their angles with c, $\varphi\boldsymbol{Sq}_i$ the phases among the various orbits (in fractions of 2π). Also given is the percentage of observed $(\boldsymbol{q}_3, \boldsymbol{q}_4)$ magnetic intensities (323).

$\lambda = 2.99$ Å T (K)	$q_{3y} = q_{4y}$	$\boldsymbol{Sq}_{\mathrm{3Ho1,Ho2}}$ $\boldsymbol{Sq}_{\mathrm{4Ho1,Ho2}}$	$\varphi\boldsymbol{Sq}_{\mathrm{4Ho2}}$	$\varphi S\boldsymbol{q}_4c^\circ_{\mathrm{Ho1}}$ $\varphi S\boldsymbol{q}_4c^\circ_{\mathrm{Ho2}}$	Int $\boldsymbol{q}_3$, $\boldsymbol{q}_4$ %	R_{B}, R_{wp}, R_{exp}%, χ^2	$R_{\mathrm{m}}\boldsymbol{q}_3\boldsymbol{q}_4$ %
1.66	0.25	3.7(1)	0.688(3)	160(1)	40	2.9, 16.2	9.7
		9.1(1)		160(1)		4.7, 11.9	
3.43	0.25	3.8(1)	0.683(3)	163(1)	39	2.8, 16.2	9.6
		8.9(1)		163(1)		5.4, 8.9	
5.35	0.2540(2)	2.98(6)	0.662(3)	8.3(5)	35	2.2, 14.1	8.4
		8.38(6)		8.3(5)		5.8, 5.9	
5.83	0.2574(3)	3.09(6)	0.664(2)	8.3(6)	37	2.6, 14.9	10.6
		8.31(6)				5.7, 6.8	
6.3	0.2591(2)	2.94(5)	0.659(2)	8.2(6)	34	2.3, 14.6	9.8
		8.25(6)				5.7, 6.5	
6.77	0.2614(3)	2.66(6)	0.660(2)	−4(1)	33	2.4, 14.7	10.0
		8.09(6)				5.8, 6.4	
7.24	0.2632(3)	2.42(6)	0.656(2)	−3(1)	31	2.0, 15.2	9.3
		7.85(6)				6.0, 6.3	

Table 6. Refinements of $HoGe_3$ HR D1A data in the HT range with wavevector $\boldsymbol{q}_2 = (q_{2x}, 0, q_{2z})$ relating to the C-cell (a, b, c) and in the LT range with (model (I)) $\boldsymbol{q} = (0, \frac{1}{4}, 0)$ relating to the enlarged P-cell $(2a, b, 3c)$. $\boldsymbol{Sq}_i$ are the Fourier coefficients and $\varphi_{Sq}c^\circ$ their angles with c, $\varphi\boldsymbol{Sq}_i$ the phases among the various orbits (in fractions of 2π). Also given is the percentage of observed $\boldsymbol{q}_2$ and $\boldsymbol{q}$ magnetic intensities (663 and 7930 reflections respectively).

$\lambda = 1.9108$ Å T (K)	q_{2x} q_{2z}	$\boldsymbol{Sq}_2$ $\varphi S\boldsymbol{q}_2c^\circ$	$\boldsymbol{Sq}_{\mathrm{Ho1-Ho2}}$ $\boldsymbol{Sq}_{\mathrm{Ho3-Ho4}}$	$\varphi\boldsymbol{Sq}_{\mathrm{Ho3}}$ $\varphi\boldsymbol{Sq}_{\mathrm{Ho4}}$	$\varphi\boldsymbol{Sq}c^\circ_{\mathrm{Ho1-Ho2}}$ $\varphi\boldsymbol{Sq}c^\circ_{\mathrm{Ho3-Ho4}}$	Int $\boldsymbol{q}_2$ Int $\boldsymbol{q}$%	R_{B}, R_{wp} R_{exp}%, χ^2	$R_{\mathrm{m}}q_2$, $R_{\mathrm{m}}q$%
1.70			11(1)	0.433(9)	42(1)		3.0, 13.7	—
			7.5(9)	0.404(12)	0	39	3.5, 15	9.5
3.47			12(1)	0.450(8)	35(1)		2.8, 12.5	—
			9.4(9)	0.436(9)	0	40	4.4, 7.8	8.0
5.42			11(1)	0.445(8)	31(1)		2.7, 12.3	—
			10(1)	0.429(9)	0	40	4.6, 7.8	7.6
7.37			7.9(1.2)		48(1)		3.0, 13.7	—
			6.8(1.1)		0	23	5.2, 6.8	12.3
8.34	0.4932(1)	6.93(4)	2.6(5)		53(14)	20	2.8, 11.1	6.3
	0.3376(1)	20(2)	1.7(1.2)			2	5.2, 4.7	15.2
9.31	0.4926(1)	6.20(4)				16.6	2.9, 11.3	6.9
	0.3383(1)	22(2)				—	5.4, 4.3	—
10.28	0.4932(1)	4.50(5)				9.8	3.5, 12.0	9.4
	0.3392(2)	26(3)				—	5.7, 4.3	—
14.0							3.6, 12.0	—
							5.9, 4.2	—

with the larger wavelength, which we present more extensively. Figure 3 compares the refined 8.08 K patterns (top part) in the IT magnetically ordered range with two coexisting magnetic phases in proportions (total intensity contributions) of 16% for $\boldsymbol{q}_2$ and 8% for $\boldsymbol{q}$ with the refined pattern in the LT state at 7.71 K where only the $\boldsymbol{q} = (0, \frac{1}{4}, 0)$ phase exists (bottom part). The refined magnetic parameters for model (I) are given in table 5a together with the results for the HT range ($\boldsymbol{q}_2$ phase). We compare these results with those obtained from refinements of the 1.9108 Å data given in table 6. We also give the results for the LT data set of table 5a refined with model (II) in table 5b.

The LT_1 range: $1.6\ K \rightarrow T_3, T_3 = 4.8\ K$. Parts of the observed and calculated neutron diffraction patterns of $HoGe_3$ (D1A 2.99 Å data) are shown in figure 4(a) above (LT_2 range) and (b) below (LT_1 range) the $T_3 = 4.8$ K SR transition at 5.5 K at 1.6 K respectively. The best fit of the LT data in terms of R_{m}% values (about 2% lower) is obtained by the refinements of the 2.99 Å data using model (I). We would like to note that the refinement converges when the moments of the atoms shifted by $(\frac{1}{4}, \frac{1}{2}, 0)$ are constrained to the same value (but opposite directions) as those for the origin and are not included in tables 5a and 6. The refined Fourier coefficients of the two D1A data sets (tables 5a and 6) change in value below 5.5 K and down to 1.6 K but their angles to the c axis are the same. In contrast to the $TbGe_3$ case, the lock-in transition in $HoGe_3$ at T_3 does not lead to an equal moment structure or to a uniaxial structure. Between the HT (figure 2) and the LT structures there is a rearrangement of the magnetic moments. In both structures some of the moments point along c, as for sublattice R_1 for the HT phase and sublattices R_3 and R_4 for the LT_1 phase (see figure 5(a)), while the moments of the R_1 and R_2 sublattices of the LT_1 phase undergo rotations within the plane (b, c).

3.3. LT_1 magnetic structures

Figure 5 displays two models of the LT_1 lock-in magnetic structures at 1.6 K. The moment values in the two plots are derived from the refined Fourier coefficients given in table 5a for model (I) (figure 5(a)) and in table 5b for model (II) (figure 5(b)) using expression (1). As already mentioned, the number of magnetic structures that can be deduced from the refined Fourier coefficients of a given model using expression (1) depends on the free choice of the global phase in the case of a single vector and of its harmonics, or of the relative phases of Fourier coefficients of symmetry independent vectors of the same basis. This information cannot be obtained using diffraction. The phase choice of the presented magnetic structures is deduced with the help of the computer program '*Moment*' by optimization of the local moment value fluctuations.

Model (I) results in a multiaxial sine wave modulated structure. As already mentioned, the 24 Ho atoms split into twelve independent magnetic sites: two fourfold, six twofold, and four single. In our calculations these are regrouped into the four sites Ho1, Ho2, Ho3 and Ho4. The best fit in this model is obtained for the modes given in table 4 and is shown in figure 5(a). The refinements indicated strong correlations of the Fourier coefficients $S\boldsymbol{q}_{\mathrm{Ho1}} \approx S\boldsymbol{q}_{\mathrm{Ho2}}$ that at 1.6 K measure 11.4 μ_{B}. Their angle to the c axis is close to $\pm\pi/4$ within the plane (b, c). The moments of atoms of the same site in planes perpendicular to the wavevector have the same value, while those in the direction of the wavevector depend on their location. Within the experimental error the wavevector length can be approximated as a fourfold cell enlargement along the b axis $\boldsymbol{q} = (0, \frac{1}{4}, 0)$.

Setting the origin of the wave on Ho1 at $(00.41\frac{1}{12})$ the atoms translated by $n\boldsymbol{t}_b$ where $n = 2m + 1$ have zero moment $S_{(q)}x\cos(2\pi/4)$. Choosing a global phase of $-\pi/4$ results in equal moment values $S_1(\boldsymbol{q})\cos(2\pi/4 - \pi/4) = S(\boldsymbol{q})\sqrt{2}/2 =$

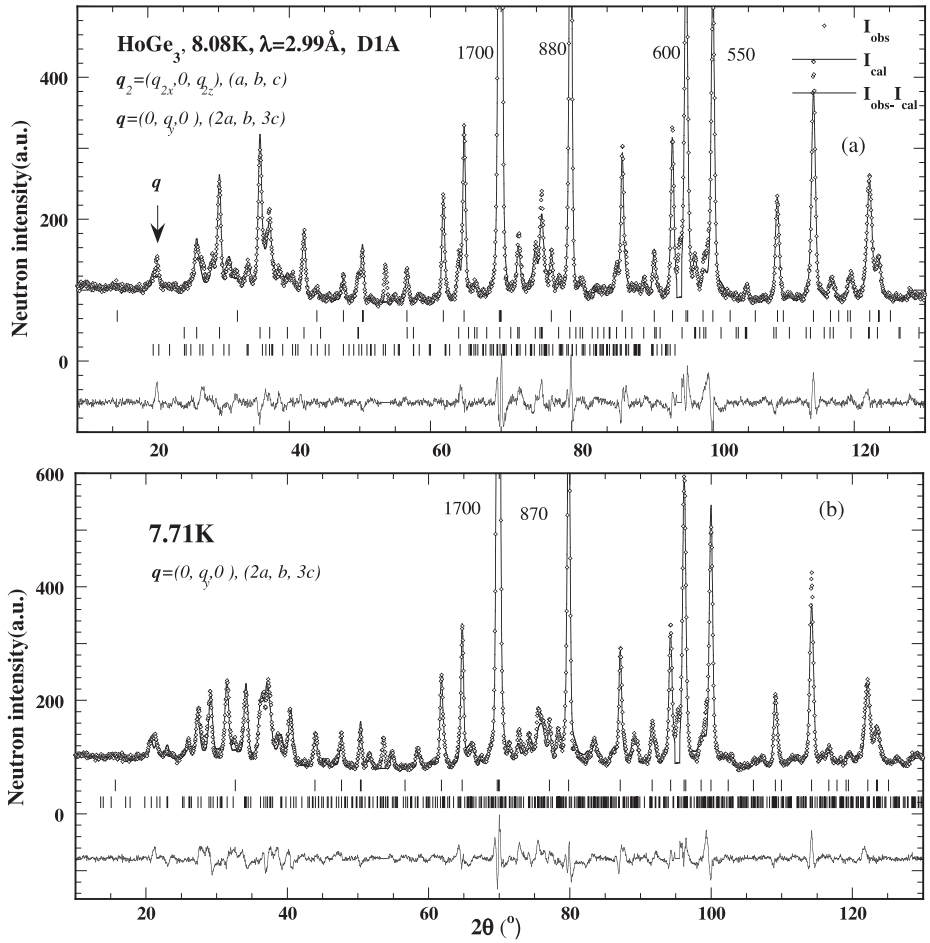

Figure 3. Parts of the observed and calculated neutron diffraction patterns of $HoGe_3$ (D1A, 2.99 Å data): in the intermediate temperature (IT) magnetically ordered state at 8.08 K, with two coexisting magnetic phases in proportions (in intensity contributions) of 16% for $\boldsymbol{q}_2$ and 8% for $\boldsymbol{q}$ and (b) in the LT_2 state at 7.71 K with only $\boldsymbol{q}$ contributions.

8.0(7) μ_B. The moments of atoms translated by $2n\boldsymbol{t}_b$ point in opposite directions.

The moment arrangement displayed in figure 5(a) for $2\times b$ cells makes use of the global phase factor $-\pi/4$. Thus the majority ($\frac{2}{3}$) of magnetic Ho atoms comprising sites (Ho1, Ho2) have a local moment value equal to 8.0(7) μ_B/Ho atom. In this arrangement the moments of Ho1 and Ho2 atoms located at the corners of a trigonal prism are almost mutually perpendicular. The third corner of the trigonal prism is occupied by atoms of the sites Ho3 and Ho4 or of those shifted by $(\frac{1}{4}, \frac{1}{2}, 0)$. Their moments are confined to the c axis and their average ordered local moment values are the same, 3.4(4) μ_B. However there are two distinct values that alternate along the direction of the wavevector (b). These are 4.5(4) μ_B and 2.8(3) μ_B for the Ho3 site and 5.0(5) μ_B and 1.7(2) μ_B for the Ho4 site. Then the average moment value of 6.5(6) μ_B/Ho atom in the cell compares favourably with the moment value of 7 μ_B obtained from the field dependent magnetic measurements at 1.8 K (see part I).

For model (II) with the symmetry independent vectors $\boldsymbol{q}_3 = (\frac{1}{2}, \frac{1}{4}, 0)$ and $\boldsymbol{q}_4 = (\frac{1}{2}, \frac{1}{4}, \frac{1}{3})$ things are more complex as there are two distinct global angles, one for each vector. The optimized global phase values Ψ_G are -0.455 and 0.379 for the two Fourier components respectively. The resulting local moments for a number of cells, $2 \times a$ $2 \times b$ $3 \times c$ (see figure 5(b)), of the two Ho sublattices vary in magnitude and in direction around c. For Ho1 the local moment scatters over 2.7 $\mu_B \rightarrow$ 10.9 μ_B and for Ho2 over 1.6 $\mu_B \rightarrow$ 10.8 μ_B. The maximum moment angle is closer to the c direction within the plane (b, c) than in the HT collinear model. This is slightly reminiscent of the fluctuating HT structure found in $TbGe_3$ although the wavevectors are completely different.

Furthermore because the star of $\boldsymbol{q}_3$ has four arms and that of $\boldsymbol{q}_4$, eight arms, one should keep in mind that the symmetry of the magnetic structure in such cases of multi-$\boldsymbol{q}$ vectors depends also on the number of branches participating in the transition that cannot be detected from neutron powder diffraction data and is not addressed in the present analysis. The magnetic structure shown in figure 5(b) is based on the summation of the Fourier components associated with a single branch of each star of the two multi-$\boldsymbol{q}$ wavevectors. The inclusion of further Fourier components associated with other branches of the wavevector star may lead to a large variety of magnetic arrangements.

Both LT models make simplifications in order to reduce the number of free parameters, as the development of a more

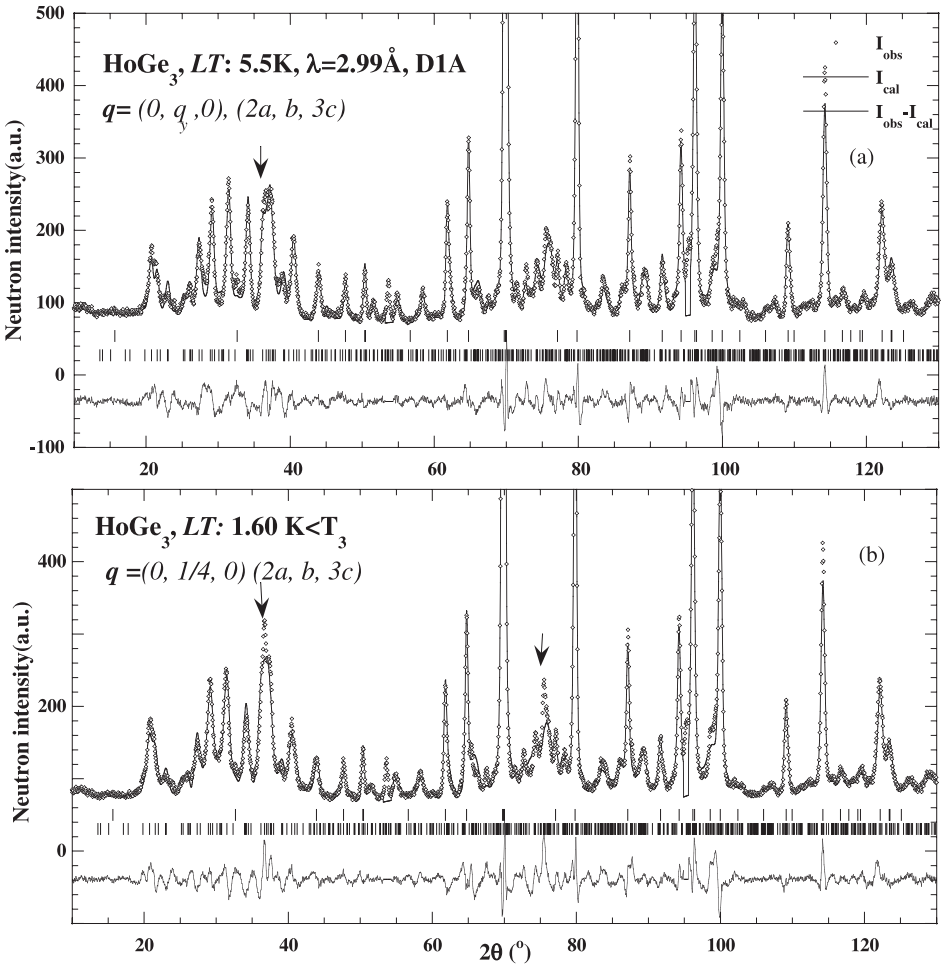

Figure 4. Parts of the observed and calculated neutron diffraction patterns of $HoGe_3$ (D1A, 2.99 Å data) (b) in the LT_2 range at 5.5 K and in the LT_1 range at 1.6 K below the SR transition at $T_3 = 4.8$ K.

general model in the 24 times larger cell is not feasible on the basis of powder diffraction. As already said, model (I) led to better fits than model (II). It also leads to the ordered moment value of 8.0 μ_B/Ho atom for $\frac{2}{3}$ of the Ho atoms below the lock-in transition. The structure shown in figure 5(a), where the atoms with the larger moments at the corners of a trigonal prism are almost perpendicular to each other, reflects the 'effort' of the system to overcome frustration [12, 13], while the moment direction of the third atom of the trigonal prism points along the c direction and its value is reduced.

Both models provide satisfactory results in the temperature range 5.5 K $\rightarrow$ 8.1 K. On the other hand, neither model provides a full explanation of the observed changes that occur below the lock-in transition at $T_3 = 4.8$ K, where the wavevector becomes commensurate. This is seen in figure 4(b) in the refinements of the 1.6 K data where the increase of the two peaks denoted by arrows is not explained by any of the models. Such details may only be answered using single-crystal data not yet available to us. Of course there is still the possibility that these peaks arise from a small amount of overlapping impurity phase peaks.

3.4. Thermal variation of the HT and LT wavevectors

Irrespective of the open questions concerning the model choice in multiple-$\boldsymbol{q}$ vector magnetic structures, our refinements enlarge the experimental information with respect to the thermal behaviour of the wavevectors. In particular, this relates to the LT range, due to the huge peak overlap. The behaviour of the LT vector could only be obtained from the refinements of the 2.99 Å data for the two models; see figure 6(a). For both models the q_y wavevector component appears at the first-order transition at T_2, where the $(\boldsymbol{q}_1, \boldsymbol{q}_2)$ HT modulated structure, instead of a lock-in to the commensurate structure $(2a, b, 3c)$, jumps to another reciprocal lattice point. The LT magnetic structure is incommensurate with the crystal lattice with a partial lock-in at T_2. The wavevector describing the LT ordering, $\boldsymbol{q} = (0, q_y, 0)$, and a six-times larger cell $(2a, b, 3c)$, varies in length with temperature. From $T_2 = 8.1$ K down to the LT lock-in transition at $T_3 = 4.8$ K, q_y decreases gradually with decreasing temperature from 0.265 to $q_y = \frac{1}{4}$.

The thermal variation of the $HoGe_3$ HT wavevector components is compared to that of the $TbGe_3$ compound in figures 6(b) and (c) as the two systems are described using the same incommensurate wavevectors $(\boldsymbol{q}_1, \boldsymbol{q}_2)$. However, even their HT structures are very different: canted fluctuating

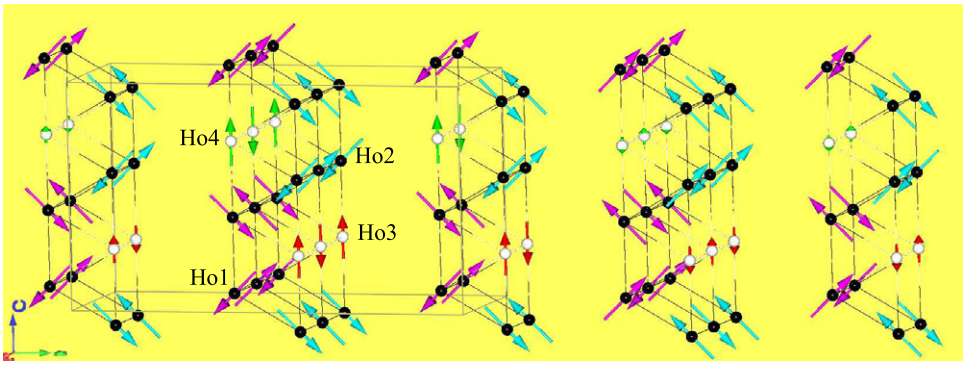

(a)

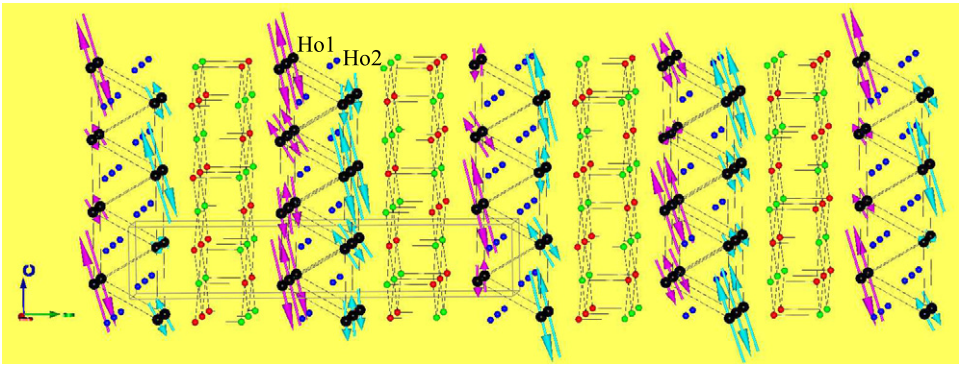

(b)

Figure 5. The canted lock-in LT_1 magnetic structure from refinements in the IC approximation of $HoGe_3$ at 1.6 K (a) for two different descriptions: (a) $(2a, b, 3c)$ and $\boldsymbol{q} = (0, \frac{1}{4}, 0)$ and (b) $\boldsymbol{q}_3 = (\frac{1}{2}, \frac{1}{4}, 0)$, $\boldsymbol{q}_4 = (\frac{1}{2}, \frac{1}{4}, \frac{1}{3})$ and the (a, b, c) cell. Only two cells are shown along the b direction.

modulated magnetic structure with the moments changing in value and direction within the plane (b, c) for $TbGe_3$ and a $\boldsymbol{q}_2$ sine wave type modulated structure with the moments confined within the plane (b, c) for $HoGe_3$, disregarding the very weak $\boldsymbol{q}_1$ contribution.

Besides the open question regarding the wavevector $\boldsymbol{q}_1$, our data indicate that also $\boldsymbol{q}_2$ displays different thermal behaviours in the two compounds. In both cases the q_{2z} component moves towards the lock-in value $\frac{1}{3}$ with decreasing temperature, though from different directions. For $HoGe_3$, $q_{2z} > \frac{1}{3}$, and therefore it decreases with decreasing temperature, while for $TbGe_3$, $q_{2z} < \frac{1}{3}$ increases. In both cases the component q_{2x} is $<\frac{1}{2}$ but its behaviours are quite different in the two compounds. In $TbGe_3$, q_{2x} over $T_N \rightarrow T_{ic}$ remains unchanged and jumps to the lock-in value $q_{2x} = \frac{1}{2}$ below T_{ic} where the structure becomes collinear and starts to square up. For $HoGe_3$, q_{2x} is seen to move slowly away from the lock-in value over $T_N \rightarrow T_1$ but its slope changes sign below $T_1 = 9.5$ K and moves smoothly towards the lock-in value in the range down to $T_2 = 8.1$ K where the first-order transition occurs. Interestingly, in the narrow intermediate (IT) range $\approx$8.1 K $\rightarrow$ 7.75 K, where $\boldsymbol{q}_2$ exists as a metastable phase, the q_{2x} component displays a steeper slope towards the lock-in value 1/2 before the $\boldsymbol{q}_2$ phase fully disappears.

From these subtle observations, combined with the fact that $\boldsymbol{q}_1$ appears also at T_1, one gets the impression that between T_1 and T_2 the lock-in mechanism of the $(\boldsymbol{q}_1, \boldsymbol{q}_2)$ $HoGe_3$ phase is similar to that of $TbGe_3$, but below T_2 it competes with a second mechanism. Our refinements show that just below T_2, when q_{2x} and q_{2z} become commensurate, $\boldsymbol{q}_2$ rotates to the reciprocal lattice point $(\frac{1}{2}, q_y, \frac{1}{3})$ where q_y is temperature dependent, and is found to vary gradually from 0.265 at 8.1 K towards 0.25 at the lock-in temperature $T_3 = 4.8$ K. A change of the wavevector direction caused by a first-order lock-in transition has also been observed by us for the orthorhombic $ErNiSi_2$ compound [14] with the $Cmcm$ space group. In this case the phase sequence is from the LT lock-in $\boldsymbol{q} = (\frac{1}{2}, 0, 0)$ to a general direction $\boldsymbol{q} = (0.1262(1), 0.022(2), 0.2273(1))$ at HT.

4. Conclusions

The existence of complex phase diagrams comprising commensurate and incommensurate HT magnetic phases and the existence of phase transitions among them in rare earth intermetallic compounds are widely observed phenomena. They arise as a result of competition between the RKKY long range exchange interaction, mediated via the conduction electrons and the crystalline field anisotropy, and small quadrupole interactions [5, 6]. In general the HT incommensurate phases for Kramers ions such as Er, Dy, Gd, Ce, Nd lock-in at low temperatures to commensurate structures because of the entropy term in the free energy [5]. This

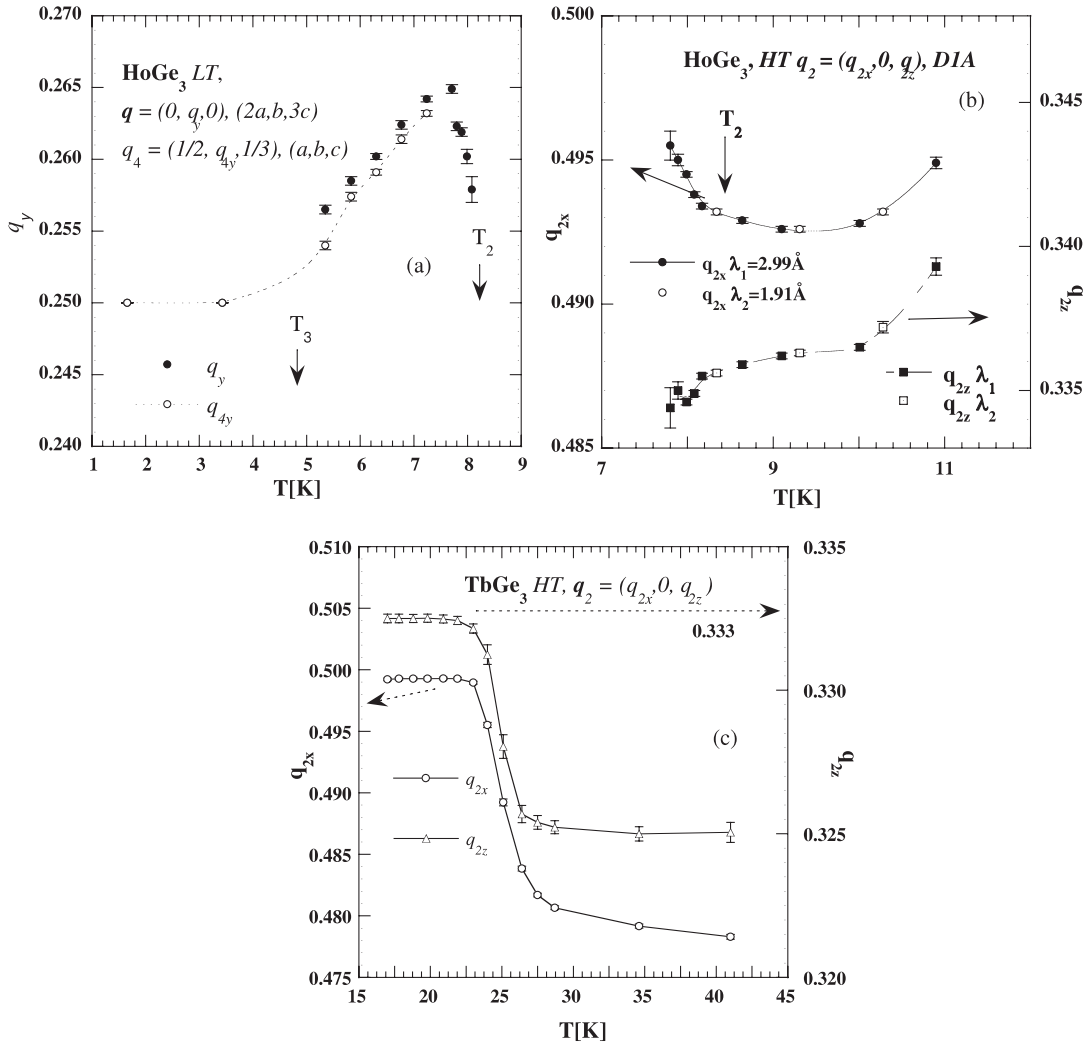

Figure 6. Thermal variation of the $\boldsymbol{q}_2$ wavevector components of the HT range of $HoGe_3$ (b) and $TbGe_3$ (c). Also shown are the thermal variations of the LT wavevector $\boldsymbol{q} = (0, q_y, 0)$ and the cell $(2a, b, 3c)$ or of $q_{3y} = q_{4y}$ in the $(\boldsymbol{q}_3, \boldsymbol{q}_4)$ relating to the (a, b, c) cell. Apparently, $HoGe_3$ undergoes at T_2 a first-order phase transition with a partial lock-in.

Table 7. Survey of the Néel (T_N) and the lock-in (T_{ic}) LT transition ordering temperatures of several RGe_3 compounds observed using neutron diffraction. Also the preferred moment directions (PMD) of the relevant sites have been listed for various wavevectors in the HT and LT ranges.

Atom/parameter	R = Tb [3]	R = Dy [10]	R = Ho	R = Er [11]
T_N (K)	40	24	12	7
Wavevectors, cell	$\boldsymbol{q}_1 = (q_{1x}, 0, 0)$, C	$\boldsymbol{q}_1 = (1/2, 0, 0)$, P	$\boldsymbol{q}_1 = (q_{1x}, 0, 0)$, C	0, C
HT	$\boldsymbol{q}_2 = (q_{2x}, 0, q_{2z})$	$\boldsymbol{q}_2 = (1/2, 0, 1/3)$	$\boldsymbol{q}_2 = (q_{2x}, 0, q_{2z})$	
PMD site R_1[a]	c	c	c	$(x, y, 0)$
PMD site R_2	$(0, y, z)\varphi_c = 30°$		$(0, y, z,)\varphi_c = 24°$	—
T_{ic} (K)	24	—	8.1	—
Wavevectors, cell	$\boldsymbol{q}_1 = (1/2, 0, 0)$, C	$\gg$	$\boldsymbol{q}_3 = (1/2, 1/4, 0)$, C	0, C
LT	$\boldsymbol{q}_2 = (1/2, 0, 1/3)$	$\gg$	$\boldsymbol{q}_4 = (1/2, 1/4, 1/3)$	
Magnetic cell V_m	$6 \times V(2a, b, 3c)$	$3 \times V((a+b)/2, (a-b)/2, c)$	$24 \times V(2a, 4b, 3c)$	V, (a, b, c)
PMD site R_1, $\mu(\mu_B)$	c, 8.1(1)	c, 8.2	c 5.3[b]	$(x, y, 0)$, 8.6
PMD site R_2 $\mu(\mu_B)$	c, 8.1(1)	c, 8.1	$(0, y, z)$11.5[b]	—

[a] For R = Er the R site does not split below T_N as $\boldsymbol{q} = 0$.

[b] For Ho these are Fourier coefficients. The Ho moments derived by the phase optimization program over the range 1.2 $\mu_B \rightarrow$ 8.0 μ_B result in six moment values depending on their position. The majority are equal to 8.0 μ_B and then 5 μ_B, and the minority are below 2 μ_B.

has been observed for all examined $R\mathrm{Ge}_3$ (R = Er, Dy, Tb) systems.

The HT ordering observed in TbGe_3 above T_{IC} is associated with (i) an incommensurate magnetic phase and the concomitant loss of symmetry and (ii) a spin reorientation transition from a uniaxial LT modulated magnetic structure with two amplitudes to a canted complex HT structure. The occurrence of canted arrangements as found in TbGe_3 may have its origin in various kinds of mechanisms such as the appearance of higher order terms in the crystalline field or of anisotropic exchange interactions of the Dzyaloshinskii–Moriya type [7, 8]. Kimura [9] found by theoretical calculations based on a 24-sublattice model for the HoCu_2 orthorhombic compound that the origin of the spin canting observed at HT was the biquadratic exchange interaction between nearest neighbour Ho ions on adjacent ac planes.

In order to understand the preferred moment direction (PMD) in these compounds we will first discuss the result obtained for site R_1. In rare earth compounds the anisotropy is usually crystal field induced and can be described by expressions of the type

$$K_1 = -2/3\alpha_J\langle r^2\rangle A_2^0\langle O_2^0\rangle - 5\beta_J\langle r^4\rangle A_4^0\langle O_4^0\rangle. \quad (3)$$

$$K_2 = 35/8\beta_J\langle r^4\rangle A_4^0\langle O_4^0\rangle. \quad (4)$$

The thermal averages of the second-and fourth-order Stevens operators are represented by $\langle O_2^0\rangle$ and $\langle O_4^0\rangle$ and the corresponding crystal field parameters are denoted by A_2^0 and A_4^0. For simplicity, we have left higher order terms out of consideration. For Tb, Dy and Ho, the Stevens coefficient α_J is negative; for Er, α_J is positive.

The thermal averages of the second-and fourth-order Stevens operators $\langle O_2^0\rangle$ and $\langle O_4^0\rangle$ fall off with temperatures as high powers of the reduced R sublattice moment $m_r = M_R(T)/M_R(0)$. It can be shown that $\langle O_2^0\rangle$ and $\langle O_4^0\rangle$ vary with temperature as m_r^3 and m_r^{10}, respectively. This means that at the higher temperatures it is reasonable to neglect the fourth-order crystal field contributions in equations (3) and (4). If we look at the PMD of R_1 sites in table 7 we see that in the HT range it is parallel to c for R = Tb, Dy, Ho but perpendicular to c for R = Er. This means that for the former three compounds one has $K_1 > 0$ whereas for R = Er one has $K_1 < 0$. Assuming a positive value of A_2^0, these results are apparently perfectly described by (the first term) of equation (3), given the fact that α_J is negative for R = Tb, Dy, Ho but positive for R = Er. Further inspection of the results displayed in table 7 reveals that in the LT range also the situation is not changed for the PMD of the R_1 site, meaning that the possible influence of the fourth-order term in equation (3) is slight, the second-order term being dominant.

Before we discuss the PMD of the R_2 sites we wish to recall that the R_1 site and R_2 site are crystallographically equivalent. This means that the crystal fields present at these sites are similar, and the values of A_2^0 (and also those of A_4^0) have to be identical. The same should be true for the anisotropy constants and the corresponding PMDs. Surprisingly this is only the case for R = Dy and Er (for R = Er one has $R_1 \equiv R_2$), and for R = Tb and R = Ho the PMD is an easy cone instead of an easy axis in the HT range. The conditions for an easy cone are $K_1 < 0$ and $K_2 > 0$, which would imply that the sign of K_1 has changed from positive for R_1 to negative for R_2. This means that a corresponding sign change must also apply for the A_2^0 values of R_1 and R_2. As we already outlined above, this is physically unrealistic because these two sites are crystallographically equivalent and their A_2^0 values should be virtually identical. Summarizing our results from the crystal field analysis we might say that experimental PMD data for site R_1 in all four compounds can be satisfactorily explained by means of crystal field theory, as exemplified by equations (3), and (4), requiring a common set of crystal field parameters in these isostructural compounds. However, the simple crystal field approach fails on extending it to the R_2 site in spite of the fact that the R_1 and R_2 sites are crystallographically equivalent.

As a possible reason for the breakdown of the simple crystal field approach we could mention that this approach is only valid if the crystal field splitting is small compared to the exchange splitting. Apparently this is not the case for site R_2. Although the sites R_1 and R_2 are crystallographically equivalent, they are not magnetically equivalent, meaning that the exchange fields are different. In fact, that is the origin of the difference between the two sites, which is closely related to the presence of magnetic frustration [12, 13] in these materials due to the particular geometric arrangement of trigonal prisms with antiferromagnetic interactions. Our conclusion is therefore that the presence of frustration in the $R\mathrm{Ge}_3$ compounds can strongly modify the crystal field interaction on crystallographically equivalent sites which, at least partially, can explain the complex magnetic ordering phenomena of these compounds.

References

[1] Rodríguez-Carvajal J 1993 *Physica* B **192** 55 The programs of the *FullProf Suite* and their corresponding documentation can be obtained from the Web at http://www.ill.eu/sites/fullprof/

[2] Chapon L C and Rodríguez-Carvajal J 2005 unpublished *FullProf Studio* is a program of the *FullProf Suite* the most recent version is freely available in the site given in [1]

[3] Schobinger-Papamantellos P, Rodriguez-Carvajal J and Buschow K H J 2007 *J. Phys.: Condens. Matter* **19** 236201

[4] Rossat-Mignod J 1987 *Methods of Experimental Physics: Neutron Scattering* vol 3 (New York: Academic)

[5] Elliott R J 1961 *Phys. Rev.* **124** 346

[6] Selke W 1988 *Phys. Rep.* **170** 213

[7] Moriya T 1960 *Phys. Rev.* **120** 91

[8] Dzyaloshinskii I E 1957 *Sov. Phys.—JETP* **5** 1259

[9] Kimura I 1990 *J. Magn. Magn. Mater.* **86** 240

[10] Schobinger-Papamantellos P, Janssen T and Buschow K H J 1996 *J. Magn. Magn. Mater.* **154** 29

[11] Schobinger-Papamantellos P, André G, Rodríguez-Carvajal J and Buschow K H J 1996 *J. Alloys Compounds* **232** 165

[12] Gignoux D and Schmitt D 2001 *J. Alloys Compounds* **326** 143

[13] Diep H T (ed) 2004 *Frustrated Spin Systems* (New Jersey: World Scientific)

[14] Schobinger-Papamantellos P, Buschow K H J, Wilkinson C, Fauth F and Ritter C 1998 *J. Magn. Magn. Mater.* **189** 214